Energy Conversion and Management 342 (2025) 120174

Contents lists available at ScienceDirect

Energy Conversion and Management

journal homepage: www.elsevier.com/locate/enconman

A sensitivity-driven thermal boundary prognostics method for assembled turbine rotor systems

Yazheng Zhao [a], Yang Zhou [a,*], Yulin Jiang [b], Jin Zhou [a], Yuanping Xu [a], Chaofeng Li [b]

[a] College of Mechanical and Electrical Engineering, Nanjing University of Aeronautics and Astronautics, Nanjing 210016, China
[b] School of Mechanical Engineering and Automation, Northeastern University, Shenyang 110819, China

ARTICLE INFO

Keywords:
Thermal boundary
Prognostics
Sensitivity-driven
Turbine rotor
Assembly system

ABSTRACT

Accurate prognostics of thermal boundaries are essential for improving the precision of temperature calculations in complex turbine rotor structures. However, existing methods often rely on extensive experimental data or demand substantial computational resources to determine thermal boundaries. This makes it difficult to balance computational efficiency and accuracy, especially when dealing with complex rotor geometries or fluctuating operating conditions. To address these challenges, this study proposes a feasible and efficient approach that integrates numerical, statistical, and iterative techniques to predict uncertain thermal boundaries in complex turbine rotors. Specifically, a precise finite element model of the assembled turbine rotor's temperature field is constructed using numerical methods. Subsequently, the temperature sensitivity of uncertain boundary parameters is evaluated by statistical methods. The key boundary parameters with high sensitivity are identified via the white shark optimizer. Based on these key parameters, the temperature distribution of the turbine rotor is predicted. Experimental results validate the high accuracy (error < 3 %) of this sensitivity-driven approach, highlighting its viability in practical scenarios where experimental data are limited but both efficiency and accuracy are essential.

1. Introduction

Accurate predictions of temperature fields are essential to ensure the reliability of turbine rotor cooling strategies and the effectiveness of thermoelastic coupled vibration control. Such accuracy requires precise thermal boundary conditions [1,2]. However, in complex structures such as aero-engine and gas turbine rotors [3], thermal boundary conditions often exhibit significant uncertainties. If these parameters cannot be predicted accurately, temperature simulation results may diverge from actual operating conditions, even when high-precision models are employed. Thus, developing effective strategies to predict uncertain thermal boundary conditions is crucial for enhancing the accuracy of temperature field reconstruction.

Extensive efforts have been made to obtain uncertain thermal boundary conditions. These approaches include data-driven models, numerical simulations, analytical methods, statistical analyses, and iterative algorithms.

(1) Data-driven models use extensive experimental datasets to predict thermal boundaries without requiring precise physical modelling. Common techniques in this category include data interpolation, deep learning, and machine learning [4–9]. Li et al. [10,11] proposed a deep learning regression-stratified strategy and distributed-coordinated neural network metamodel to improve the computational efficiency and accuracy of turbine bladed disk life assessment. Although these methods eliminate the requirement for physical models, they are highly dependent on large datasets, which constrains their adaptability to different conditions.

(2) Numerical methods have been widely applied to capture thermal boundaries. Liao et al. [12] employed computational fluid dynamics to analyze heat transfer coefficients within a rotor–stator disk cavity. Hölz et al. [13] conducted computational fluid dynamics—conjugate heat transfer simulations to evaluate various thermal boundary conditions. Martins et al. [14] used the thermal lattice Boltzmann method to calculate Neumann boundary conditions. These numerical approaches are effective for solving complex problems. However, these methods require accurate modelling and uncertainties in parameters such as inlet flow, pressure, and fluid properties may persist throughout the simulation, potentially influencing the results.

(3) Analytical methods have been used to establish theoretical solutions for thermal boundaries. Heinze et al. [15] derived an analytical

* Corresponding author at: College of Mechanical and Electrical Engineering, Nanjing University of Aeronautics and Astronautics, Nanjing, 210016, China.
E-mail address: zhouyang0216@nuaa.edu.cn (Y. Zhou).

https://doi.org/10.1016/j.enconman.2025.120174
Received 10 March 2025; Received in revised form 30 June 2025; Accepted 4 July 2025
Available online 9 July 2025

lower bound for the heat transfer coefficient, while Battaglia et al. [16] proposed an analytical approach based on mathematical modelling and fractional-order integral theory to solve thermal boundary problems. Li et al. [17] introduced assumptions of temperature boundary conditions. Liu et al. [18] directly derived an analytical solution for the thermal boundary. However, the heat transfer coefficient remains an uncertain parameter, as it depends on environmental and operating conditions, making it challenging to define accurately using analytical methods.

(4) Statistical analyses have been employed to determine thermal boundaries using probabilistic methods. Yang, Gaaloul, and da Silva et al. [19–21] employed statistical methods to calculate uncertain thermal boundaries. While these methods help account for variability, they rely on statistical assumptions and are computationally complex.

(5) Iterative algorithms have gained increasing attention in recent years owing to their effectiveness in handling complex boundary conditions and structures. Wang et al. [22] proposed a thermal boundary prognostics method based on particle swarm optimization and finite element method. Song et al. [23] incorporated physical mechanisms into the multi-objective problem for the reliability assessment of turbine blades and proposed an extreme multi-domain transformation for dataset processing, significantly reducing computational complexity. Ren and Chen et al. [24,25] applied other intelligent optimization algorithms to determine thermal boundaries. Tourn, Chen, Cui, and Duda et al. [26–31] used gradient-based methods to predict thermal boundaries. Frąckowiak et al. [32] introduced the Trefftz numerical function to solve the inverse heat conduction problem. Mierzwiczak and Wang et al. [33,34] used regularization methods to solve for thermal boundaries, while Bauzin et al. [35] employed deformation measurements for inverse thermal boundary identification. However, this method is challenged by the complex thermoelastic coupling transfer function between deformation and temperature, which demands high accuracy in both the temperature field and dynamics models.

In summary, substantial progress has been made in determining thermal boundaries. Techniques such as interpolation fitting, data-driven machine learning, numerical simulations, analytical methods, statistical methods, and iterative algorithms are widely employed. However, key technical gaps remain: most current thermal boundary estimation methods either require dense measurement data or assume idealized, uniformly distributed boundary conditions. These assumptions are often impractical for assembled turbine rotors owing to their complex structures, uncertain thermal contact characteristics, and limited accessibility for sensor placement. Moreover, the influence of each thermal boundary on the overall temperature distribution is rarely quantified prior to inversion, leading to inefficient parameter estimation and possible convergence to physically unrealistic results. In this context, the core problem addressed in this work is: how to accurately and efficiently estimate uncertain thermal boundary conditions in assembled turbine rotors using only sparse experimental data.

This study proposes a sensitivity-driven method for predicting uncertain thermal boundaries in assembled turbine rotors. The method integrates the advantages of numerical, statistical, and iterative approaches to predict thermal boundaries using sparse experimental data. This method is the primary innovation and contribution of the study. Specifically, the finite element method is used to construct a physical model of the temperature field for the turbine rotor substructures. Thermal contact resistance (TCR) is then applied to assembly substructures, obtaining an accurate temperature field model for the assembled turbine rotor. Based on this model, a quantitative sensitivity analysis of all uncertain thermal boundaries is conducted to identify highly sensitive thermal boundary parameters. The white shark optimizer (WSO) algorithm is subsequently employed to perform inverse prediction of these high-sensitivity parameters. Finally, the predicted thermal boundaries are validated by substituting them into the temperature field model and comparing the results with experimental results.

2. Assembled turbine rotor system and experimental setup

This section describes the assembled turbine rotor system and the experimental setup. First, the assembled turbine rotor structure used for thermal boundary prognostics is presented. Subsequently, the heating device and temperature data acquisition system are introduced. Finally, experimental data collected under different operating conditions are provided.

2.1. Assembled turbine rotor system

The geometric structure used in this study is a simplified design inspired by the characteristics of the GE T700 turbine rotor, rather than a full-scale replica of the actual rotor. The primary purpose of employing the simplified rotor structure is to validate the feasibility of the proposed thermal boundary prognostics method under experimentally controllable conditions, rather than to conduct a comprehensive thermal simulation of a real turbine engine.

As shown in Fig. 1(a), the actual turbine rotor is assembled from three components with a complex structure [36]. To enable practical simulation and experimental investigations, a simplified assembled rotor is developed based on dimensional analysis [37]. This design retains key geometric features while ensuring that the dynamic response reflects the essential characteristics of the actual rotor. As shown in Fig. 1(b), the simplified model is also comprised of three substructures connected by two assembly contact interfaces. Fig. 2 shows the test rig constructed with the simplified assembled rotor.

The modal assurance criterion (MAC) is calculated to quantify the similarity between mode shapes [38]:

$$MAC = \frac{\left(\phi_{FE}{}^{i}\phi_{X}{}^{j}\right)^{2}}{\left(\phi_{FE}{}^{i}\phi_{FE}{}^{j}\right)\left(\phi_{X}{}^{i}\phi_{X}{}^{j}\right)} \tag{1}$$

where $\phi_{FE}{}^{i}$ denotes the i-th mode shape of the full-scale model, and $\phi_{X}{}^{j}$ represents the j-th mode shape of the scaled rotor model. MAC values range from 0 to 1, with values close to 1 indicating strong similarity between mode shapes. As shown in Table 1, the first three modes all exceed 0.91, and their corresponding critical speeds are proportionally reduced.

The edges of the turbine disk are in direct contact with high-temperature gas, while the sides of the disk are exposed to cooling gas, resulting in a specific temperature gradient. As shown in Fig. 3, this turbine rotor includes 19 uncertain thermal boundaries.

2.2. Heating device

A circumferentially wrapped heating structure is designed (Fig. 4), incorporating a quartz lamp as the heating actuator. Combined with the temperature control and data acquisition system (Fig. 5), this setup enables precise temperature regulation.

As shown in Fig. 5, the temperature control process begins by acquiring voltage signals from the temperature sensors, which are sent to the transmitter. The transmitter processes these signals and forwards them to the dSPACE controller. Finally, the controller outputs control signals to the actuator, ensuring a circumferentially uniform temperature field for the experiment.

2.3. Experimental data collection results

Fig. 6 shows the schematic and experimental setup for the temperature sensor layout. Temperature measurements are taken at nine locations on the turbine rotor surface to support thermal boundary prognostics and validation. The sensor locations include the shaft, small drum, small disk, large drum, large disk, and internal cavity.

The proposed method in this study is applicable to both stationary and rotating structures. However, preliminary validation is carried out

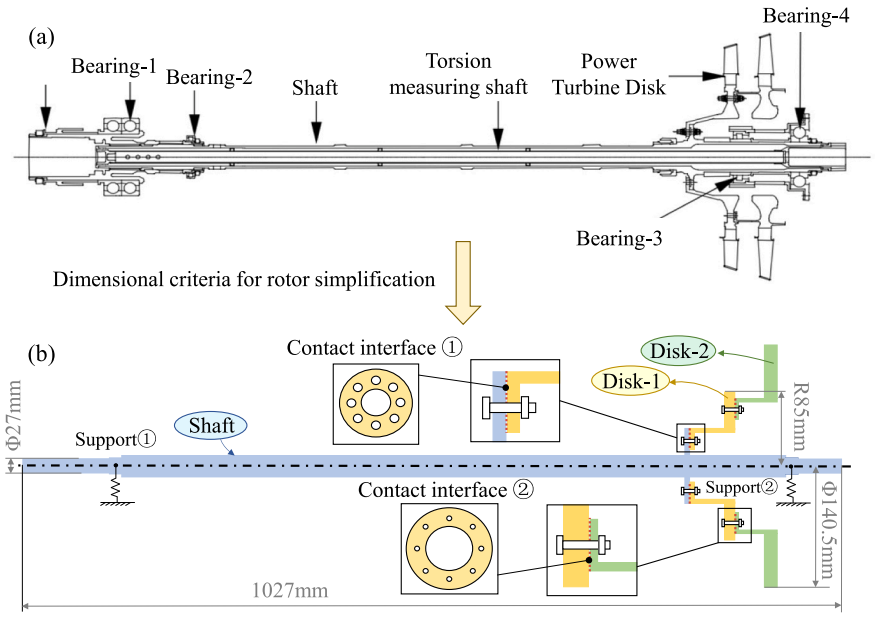

Fig. 1. Assembled turbine rotor system before and after simplification.

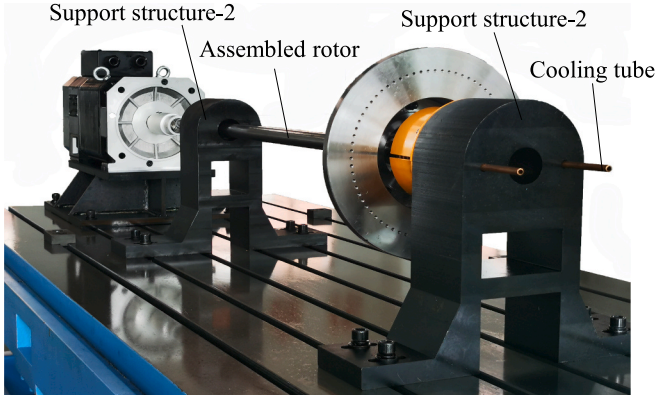

Fig. 2. The test rig of simplified assembled rotor.

Table 1
Comparison of dynamic characteristics between full-scale and scaled models.

Mode	MAC	Critical Speed (rpm) Rotor before simplification	Simplified rotor	Speed Ratio
First order	0.937	7894	3848	1:0.487
Second order	0.929	14,971	7483	1:0.499
Third order	0.910	38,683	19,689	1:0.509

using a stationary rotor owing to current limitations in temperature measurement under rotating conditions. Consequently, two steady-state non-rotating cases are selected for subsequent analysis. Figs. 7 and 8 show the temperatures recorded at the nine measurement points under these two conditions.

To minimize the impact of temperature fluctuations on prediction and validation, 5,000 temperature samples collected over 50 s are averaged. The mean temperatures at these locations under the two conditions are shown in Tables 2 and 3. These data are used for thermal boundary prognostics and validation in Section 5.

The main difference between the two cases is that Case 2 features a larger cooling hole at the left end of the heating structure compared with Case 1. Fig. 9(a) and 9(b) show the left end of the heating structure under Cases 1 and 2, respectively.

3. The temperature field model of the assembled turbine rotor

This section first presents the temperature field model of each substructure, followed by an introduction to the TCR at the bolted interfaces. The substructure models are then assembled using the TCR to construct the temperature field model of the assembled turbine rotor.

3.1. The temperature field of the substructure

The transient heat transfer in the axisymmetric structure is governed by the following partial differential equation:

$$\frac{\partial T}{\partial t}=\frac{k}{c_p\rho}\left(\frac{\partial^2 T}{\partial r^2}+\frac{1}{r}\frac{\partial T}{\partial r}+\frac{\partial^2 T}{\partial z^2}+\frac{q_v}{k}\right) \tag{2}$$

where T represents the temperature field, t denotes time, z and r are the axial and radial coordinates of the axisymmetric structure respectively, q_v represents the internal heat source, k denotes the thermal conductivity, c_p represents the constant pressure specific heat, and ρ is the density.

Based on the finite element method, the axisymmetric heat transfer equation of an element is formulated as:

$$\boldsymbol{K}(h)^E\boldsymbol{T}^E+\boldsymbol{N}^E\frac{\partial \boldsymbol{T}^E}{\partial t}=\boldsymbol{P}^E(h) \tag{3}$$

where $\boldsymbol{T}^E$ and $\{\partial \boldsymbol{T}/\partial t\}^E$ represent the temperature vector and the first-order derivative vector of temperature for an element, respectively. $\boldsymbol{K}(h)^E$, $\boldsymbol{N}^E$, and $\boldsymbol{P}(h)^E$ denote the thermal conductivity matrix, heat capacity matrix, and temperature load vector of an element, respectively. For the convective heat transfer boundary conditions, both the thermal conductivity matrix $\boldsymbol{K}^E$ and the temperature load vector $\boldsymbol{P}^E$ (shown in Appendix A) are influenced by the heat transfer coefficient h and ambient temperature T_f. Heat transfer in turbine rotors primarily occurs through convection. However, because this study uses radiation heating in the experiment, the radiation boundary condition is linearized to approximate convective heat transfer. The linearized thermal radiation boundary condition includes an equivalent heat transfer coefficient h,

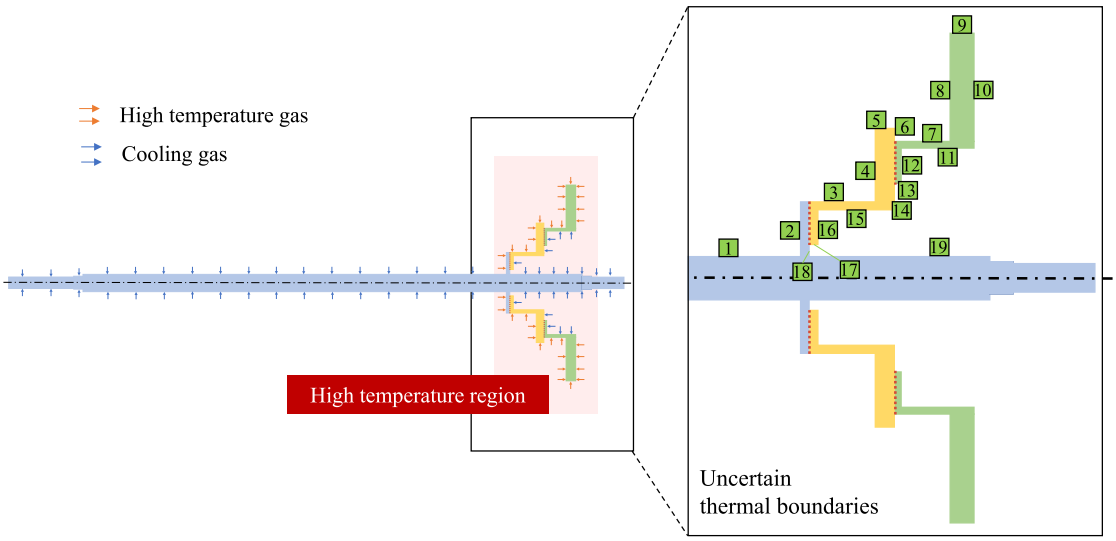

Fig. 3. Uncertain thermal boundaries of the turbine rotor.

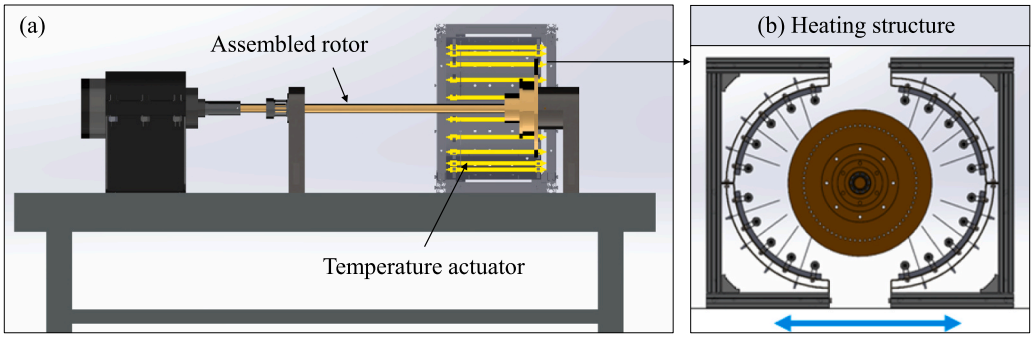

Fig. 4. Heating device.

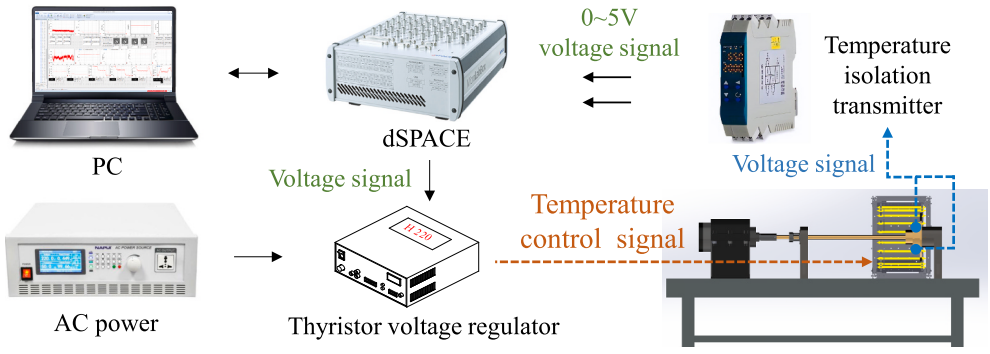

Fig. 5. Temperature control and data acquisition system.

treated as a constant under steady-state temperature conditions, and an effective radiation temperature T_f. The finite element model of the temperature field for the three substructures can be expressed as follows:

$$\begin{cases} \boldsymbol{K}_S \boldsymbol{T}_S + \boldsymbol{N}_S \dfrac{\partial \boldsymbol{T}_S}{\partial t} = \boldsymbol{P}_S \\ \boldsymbol{K}_{D_1} \boldsymbol{T}_{D_1} + \boldsymbol{N}_{D_1} \dfrac{\partial \boldsymbol{T}_{D_1}}{\partial t} = \boldsymbol{P}_{D_1} \\ \boldsymbol{K}_{D_2} \boldsymbol{T}_{D_2} + \boldsymbol{N}_{D_2} \dfrac{\partial \boldsymbol{T}_{D_2}}{\partial t} = \boldsymbol{P}_{D_2} \end{cases} \tag{4}$$

where the subscripts S, D_1, and D_2 denote the shaft, disk 1 and disk 2, respectively.

3.2. Thermal contact resistance connected by bolts

As shown in Fig. 10, when heat transfers across a contact interface, a temperature gradient develops owing to the presence of TCR. For a bolted connection, the TCR is defined as [39]:

$$R_{bolti} = \int_{a_s}^{a_{tc}} \frac{\sqrt{\pi}\xi_1 + \xi_2}{2k^2\sqrt{A_a}a_t n(a_t)} da_t + \int_{a_{tc}}^{a_{tmax}} \frac{\sqrt{2\pi}\xi_1 + 2\xi_2}{2k^2\sqrt{A_a}a_t n(a_t)} da_t \tag{5}$$

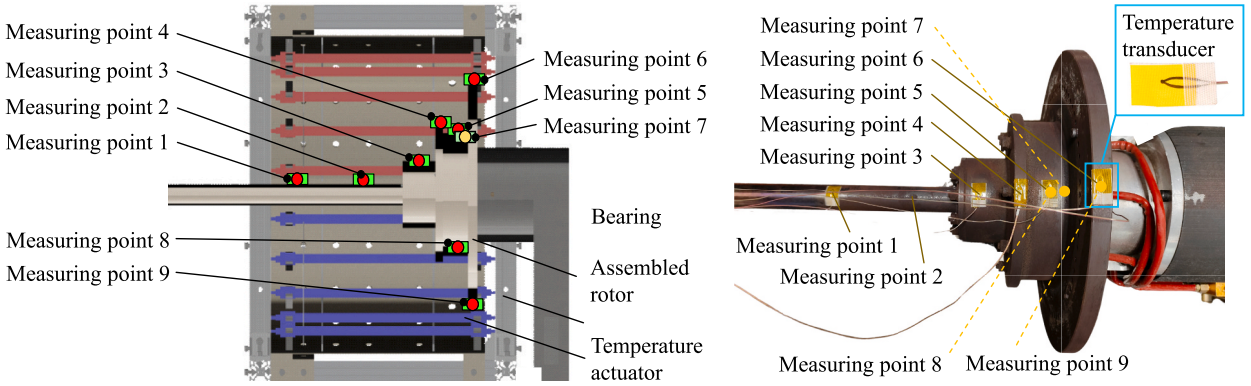

(a) Schematic diagram (b) Experimental setup

Fig. 6. Temperature sensor layout.

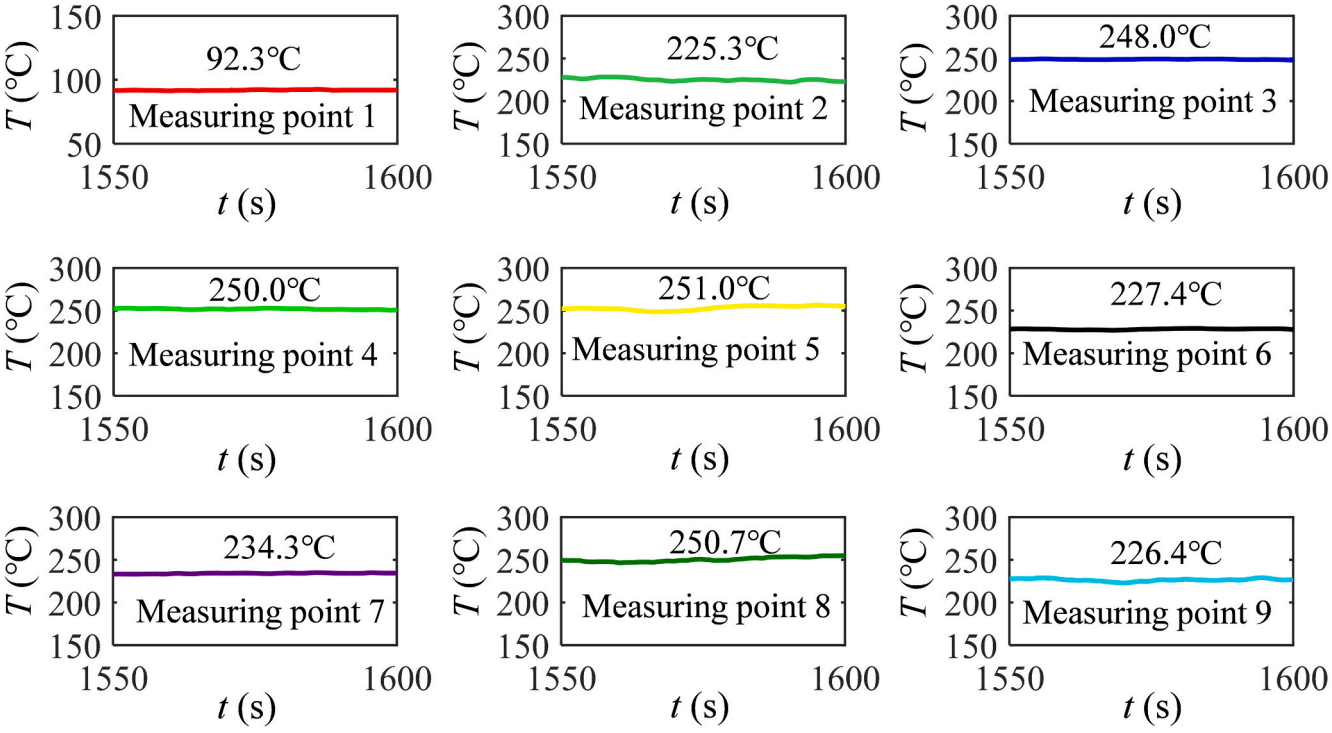

Fig. 7. Experiment data under Case 1.

where n is the asperity distribution density, k is the thermal conductivity coefficients of the structures, and A_a is the nominal contact area. a_t, a_{tmax}, a_{tc}, and a_s denote the truncated area, maximum truncated area, critical truncated area, and minimum truncated area of the asperity, respectively. Their specific definitions are provided in Appendix B. The coefficients ξ_1 and ξ_2 are defined as:

$$\begin{cases} \xi_1 = 2\sqrt{a_t A_a}\,k\left(1-\sqrt{\dfrac{A_r}{A_a}}\right)^{1.5} \\ \xi_2 = 2\sqrt{2A_r}\,k\sigma\left[erfc^{-1}(2P_s)+erfc^{-1}\left(\dfrac{2A_t}{A_a}\right)\right] \end{cases} \tag{6}$$

where σ represents the root mean square height, while A_r and A_t denote the total actual contact area and the total truncated contact area of a single bolt. The specific expressions are provided in Appendix B.

3.3. The temperature field of the assembled turbine rotor

Thermal contact conductance (TCC) represents the heat flux conducted per unit area and per unit temperature difference across the contact interface, and it is the reciprocal of TCR. The temperature field model of the assembled rotor is constructed by assembling the temperature field models of the three substructures using TCC.

$$\boldsymbol{K}\cdot\boldsymbol{T}+\boldsymbol{N}\cdot\frac{\partial \boldsymbol{T}}{\partial t}=\boldsymbol{P} \tag{7}$$

where $\boldsymbol{K}$, $\boldsymbol{N}$, and $\boldsymbol{P}$ are the thermal conductivity matrix, heat capacity matrix, and temperature load vector of the assembled rotor, respectively. The temperature model of the assembled rotor is discretized using triangular finite elements, comprising 1,404 nodes and 2,128 elements.

For the steady-state heat conduction problem, a direct solver based on Cholesky decomposition is employed to solve the linear system. The governing equation is expressed as:

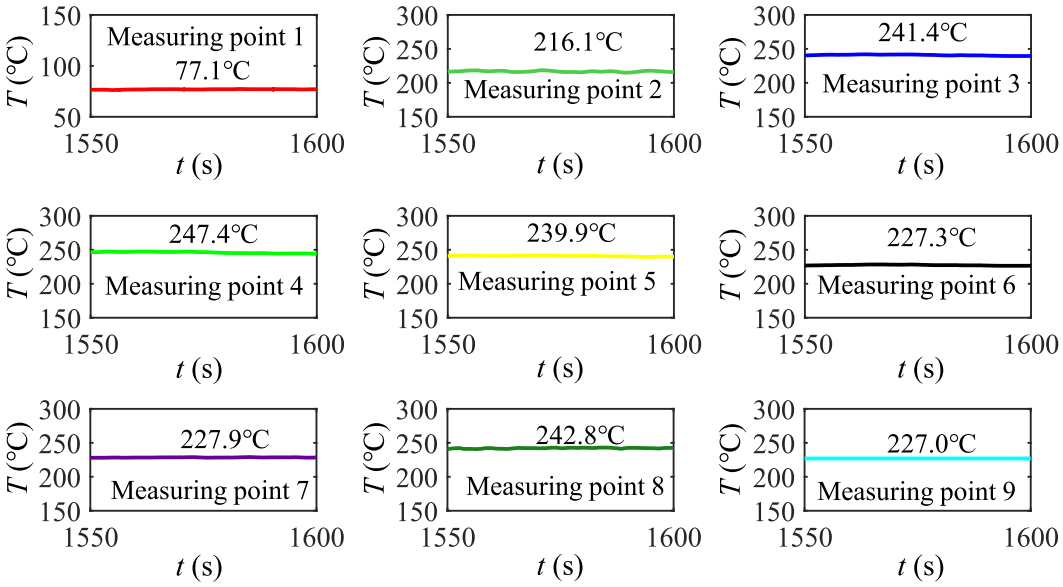

Fig. 8. Experiment data under Case 2.

Table 2
Experiment temperature values under Case 1.

Type	Temperature (°C)	Type	Temperature (°C)	Type	Temperature (°C)
Measuring point 1	92.3	Measuring point 4	250.0	Measuring point 7	234.3
Measuring point 2	225.3	Measuring point 5	251.0	Measuring point 8	250.7
Measuring point 3	248.0	Measuring point 6	227.4	Measuring point 9	226.4

Table 3
Experiment temperature values under Case 2.

Type	Temperature (°C)	Type	Temperature (°C)	Type	Temperature (°C)
Measuring point 1	77.1	Measuring point 4	247.4	Measuring point 7	227.9
Measuring point 2	216.1	Measuring point 5	239.9	Measuring point 8	242.2
Measuring point 3	241.4	Measuring point 6	227.3	Measuring point 9	227.0

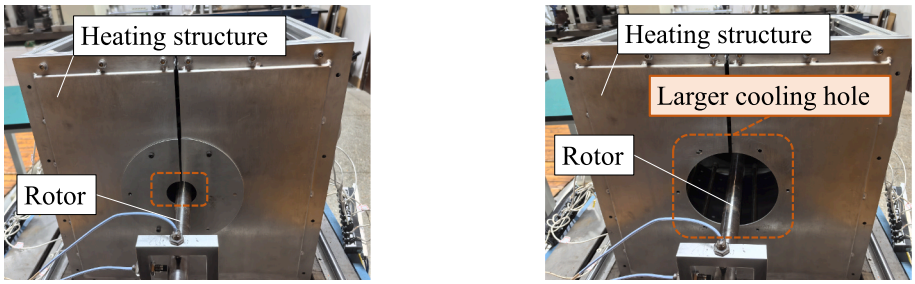

(a) Case 1 (b) Case 2

Fig. 9. Left end of the heating structure under two cases.

$$\boldsymbol{T} = \frac{\boldsymbol{P}}{\boldsymbol{K}} \tag{8}$$

For the transient heat conduction problem, Galerkin time discretization based on the weighted residual method is employed. The corresponding computational equation is given by:

$$\left(2\boldsymbol{K} + \frac{3\boldsymbol{N}}{\Delta t}\right)\boldsymbol{T}_t = 2\boldsymbol{P}_t + \boldsymbol{P}_{t-\Delta t} + \left(\frac{3\boldsymbol{N}}{\Delta t} - \boldsymbol{K}\right)\boldsymbol{T}_{t-\Delta t} \tag{9}$$

where Δt is the time step, which is set to 0.01 s.

3.4. The parameters of the temperature model

The assembled rotor includes two bolted contact interfaces, as shown in Fig. 11. Table 4 lists the structural and material parameters used to calculate the temperature distribution. Aside from the fractal dimension and fractal roughness derived from experimental data [40–42], all other parameters are obtained from material properties, rotor geometry, or

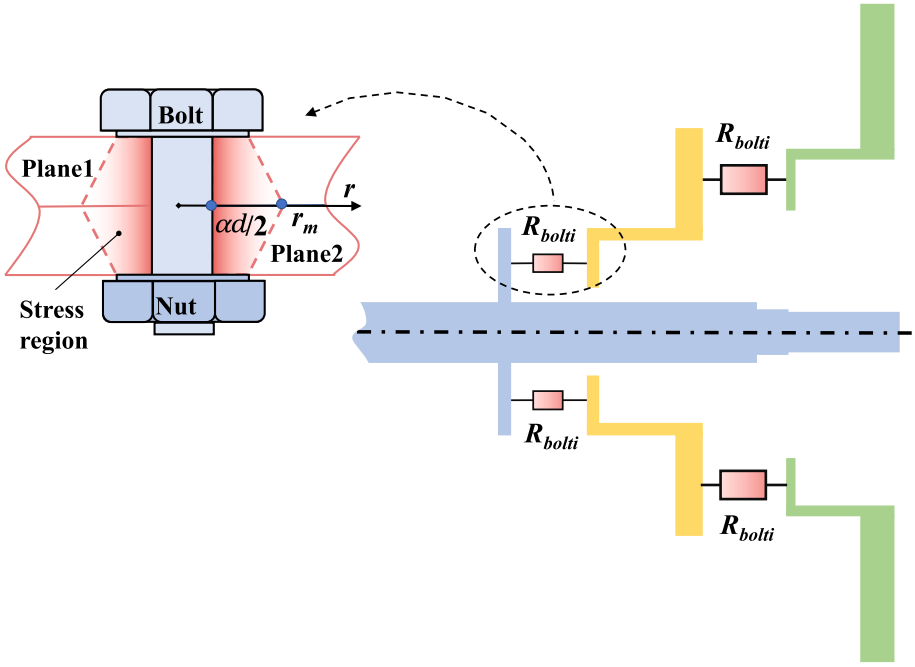

Fig. 10. The thermal resistance equivalent method.

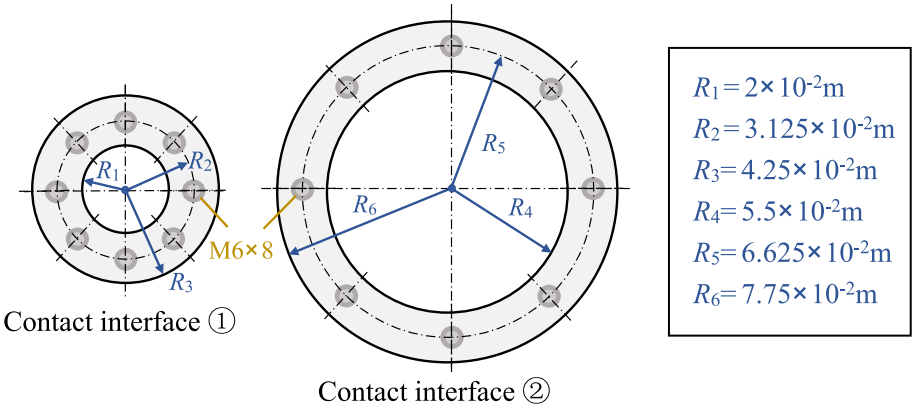

Fig. 11. Contact interfaces.

Table 4
Structural and material parameters of two contact interfaces.

Parameters	Value	Parameters	Value
Fractal dimension of interfaces D_f	1.6182	RMS height σ	1.56 × 10^{-6}
Fractal roughness of interfaces G_f	4.1252 × 10^{-7}	Small probability value P_s	0.05
Equivalent hardness $\widetilde{H}$	2.04 GPa	Nominal contact area of interface ①A_a	4.4 × 10^{-3} m^2
Equivalent elastic modulus $\widetilde{E}$	108 GPa	Nominal contact area of interface ②A_a	0.011 m^2
Bolts number of interfaces N_{bolt}	8	Thermal conductivity k	50 W/m·K
Bolt hole inner diameter d	0.006 m	Bolt hole diameter coefficient α	1.125

empirical formulas.

Additionally, based on the radiation efficiency and characteristics of the quartz heating lamps used in experiments, the effective radiation temperature is first estimated. The corresponding results are shown in the Table 5.

Table 5
Effective radiation temperature.

Parameter	Effective radiation temperature (℃)
C_1, C_{19}	27
C_2, C_4, C_6, C_8, C_{10}, C_{11}, C_{12}, C_{13}, C_{14}, C_{15}, C_{16}, C_{17}, C_{18}, C_{19}	100
C_3, C_5, C_7, C_9	320

4. Thermal boundary sensitivity analysis of the assembled turbine rotor

This section first introduces the variance-based methods used for uncertainty and sensitivity analysis. Next, the temperature objective functions are defined. Finally, the sensitivity of thermal boundaries to the objectives is analyzed in detail to identify boundaries with high sensitivity.

4.1. Sensitivity analysis method

For a temperature objective function $T_{ob} = f(C_1, C_2, ..., C_{19})$, where $C_1, C_2, ..., C_{19}$ represent multiple uncertain boundaries, variance-based sensitivity analysis is applied. This method entails a comprehensive decomposition of the uncertainty associated with T_{ob}. The variance $V(T_{ob})$ of the objective function can be expressed as:

$$V(T_{ob}) = \sum_{i=1}^{nC} V_i + \sum_{i=1}^{nC}\sum_{j=i+1}^{nC} V_{ij} + \cdots + V_{12\cdots nC} \tag{10}$$

where V_i represents the contribution of input C_i to total variance $V(T_{ob})$, while V_{ij} denotes the contribution of the interaction between C_i and C_j. The term $V_{12,\cdots,nC}$ accounts for the contribution from higher-order interactions among all input variables $C_1, C_2, ..., C_{nc}$. To quantify the influence of C_i on the output variance, the first-order sensitivity index is defined as:

$$S_i = \frac{V_i}{V(T_{ob})} = \frac{V_{C_i}\left(E_{C_{\sim i}}(T_{ob}|\boldsymbol{C}_i)\right)}{V(T_{ob})} \tag{11}$$

To quantify both the first-order and higher-order effects of C_i on the variance $V(T_{ob})$, the variance-based global sensitivity index is defined as:

$$S_{Ti} = \frac{V_i + \sum_{j=1 j\neq i}^{nC} V_{ij} + \cdots + V_{12\cdots nC}}{V(T_{ob})} = \frac{E_{C_{\sim i}}\left(V_{C_i}(T|\boldsymbol{C}_{\sim i})\right)}{V(T)} \tag{12}$$

where $\boldsymbol{C}_i$ represents the sample matrix of the factor C_i, while $\boldsymbol{C}_{\sim i}$ denotes the sample matrix for all factors except C_i. The variance $V_{C_i}(E_{C_{\sim i}}(T_{ob}|\boldsymbol{C}_i))$ and the mean $E_{C_{\sim i}}(V_{C_i}(T_{ob}|\boldsymbol{C}_{\sim i}))$ are computed from the sample matrices and the temperature field model. These values are then substituted into Eqs. (10) and (11) to determine the sensitivity indices. To calculate the variance and mean efficiently, the improved method proposed by Saltelli et al. [43] is employed:

$$\begin{cases} V_{C_{\sim i}}\left(E_{C_i}(T_{ob}|\boldsymbol{C}_{\sim i})\right) = \dfrac{1}{N}\sum_{j=1}^{N} f(\boldsymbol{B})_j\left(f\left(\boldsymbol{A}_{\boldsymbol{B}}^{(i)}\right)_j - f(\boldsymbol{A})_j\right) \\ E_{C_{\sim i}}\left(V_{C_i}(T_{ob}|\boldsymbol{C}_{\sim i})\right) = \dfrac{1}{2N}\sum_{j=1}^{N}\left(f(\boldsymbol{A})_j - f\left(\boldsymbol{A}_{\boldsymbol{B}}^{(i)}\right)_j\right)^2 \end{cases} \tag{13}$$

Therefore, the first-order sensitivity and the global sensitivity indices are expressed as follows:

$$\begin{cases} S_i = \dfrac{\sum_{j=1}^{N} f(\boldsymbol{B})_j\left(f\left(\boldsymbol{A}_{\boldsymbol{B}}^{(i)}\right)_j - f(\boldsymbol{A})_j\right)}{NV(T)} \\ S_{Ti} = \dfrac{\sum_{j=1}^{N}\left(f(\boldsymbol{A})_j - f\left(\boldsymbol{A}_{\boldsymbol{B}}^{(i)}\right)_j\right)^2}{2NV(T)} \end{cases} \tag{14}$$

where $\boldsymbol{A}$ and $\boldsymbol{B}$ are two independent sampling matrices, i represents the i-th factor ($i \in [1, nC]$), and j denotes the number of simulation ($j \in [1, nS]$). To calculate the variance and mean, the matrix $\boldsymbol{A}_{\boldsymbol{B}}^{(i)}$ is introduced, with its detailed definition provided in Appendix C.

Variance-based sensitivity analysis employs 5,000 input samples generated through latin hypercube sampling to ensure a comprehensive and uniform exploration of the parameter space. Convergence is considered achieved when incremental increases in sample size result in fluctuations of first-order and global sensitivity indices less than 1 %, serving as a criterion for result stability and reliability.

4.2. Sensitivity objective function

To avoid introducing subjectivity or unnecessary bias from artificially assigned weighting factors, a simple summation method is used to define the objective function for sensitivity analysis. This approach ensures consistent treatment of temperatures across different regions, facilitating an objective evaluation of the model's temperature response throughout the entire boundary. It also enables more effective identification of sensitive boundary parameters that significantly influence overall performance.

When analyzing the temperature at each node of the turbine rotor, it is essential to evaluate the influence of uncertain boundary parameters on the first temperature objective function defined in Eq. (15).

$$T = \sum_{i=1}^{N_{node}} T(i) \tag{15}$$

where N_{node} denotes the total number of nodes in the rotor's temperature field model, and $T(i)$ represents the temperature at the i-th node. When focusing on temperatures at specific critical locations on the turbine rotor surface, a second temperature objective function is defined as follows:

$$T = \sum_{i=1}^{M_{node}} T(i) \tag{16}$$

where M_{node} denotes the number of critical points.

4.3. Sensitivity analysis of the thermal boundary

The uncertainty and sensitivity of thermal boundaries are analyzed. Fig. 12 illustrates the probability distribution histogram of the first temperature objective function, which exhibits an asymmetric distribution centered around 116 °C, with a peak frequency of approximately 0.06, indicating a concentrated distribution.

The scatter plots in Fig. 13 reveal a strong correlation between boundary C_9 and the output temperature, indicating its significant influence on the objective function.

To quantitatively evaluate the sensitivity of uncertain thermal boundaries, first-order and global sensitivity analyses are conducted, as shown in Figs. 14 and 15. The first-order and global sensitivity indices of boundary C_9 dominate, accounting for 66.45 % and 62.71 %, respectively, followed by C_5 (11.3 % and 14.61 %) and C_{10} (12.13 % and 11.24 %). These results indicate that boundaries C_5, C_9, and C_{10} have a greater impact on the output temperature than the other boundaries.

The uncertainty and sensitivity of thermal boundary conditions are evaluated with respect to the temperature at critical locations on the rotor surface. As shown in Fig. 16, the probability histogram of the temperature distribution follows a symmetric normal distribution centered at 216.2 °C with a peak probability of 0.074.

The scatter plots in the Fig. 17 indicate that boundary C_3 exhibits a weak correlation with the temperature objective function, while the other boundaries show no discernible correlation.

To further quantify sensitivity, a variance-based sensitivity analysis is conducted. As shown in Fig. 18, the first-order sensitivity indices of boundaries C_3, C_5, C_7, C_9, C_{10}, and C_{15} are 38.43 %, 10.63 %, 9.73 %, 11.31 %, 6.05 %, and 17.47 %, respectively, while the remaining boundaries have negligible influence on the output. The global sensitivity analysis, illustrated in Fig. 19, shows that the global sensitivity

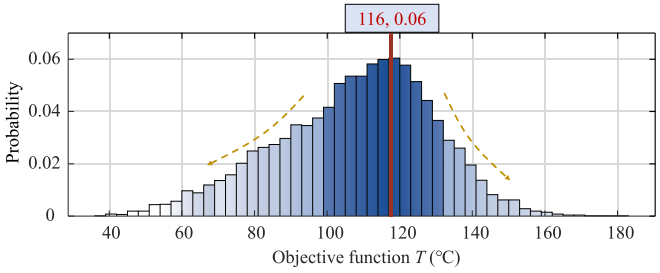

Fig. 12. Probability distribution of the first temperature objective function.

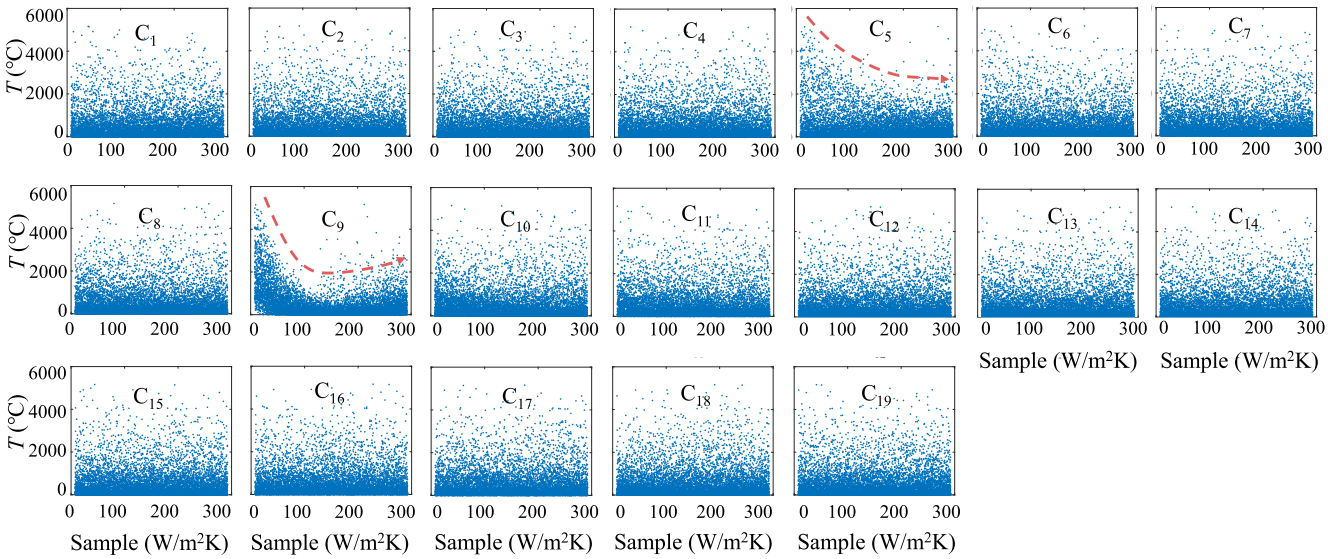

Fig. 13. Scatter plot of the first temperature objective function.

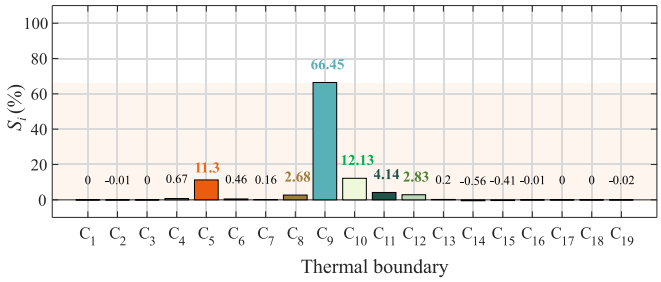

Fig. 14. First-order sensitivity of uncertain thermal boundaries.

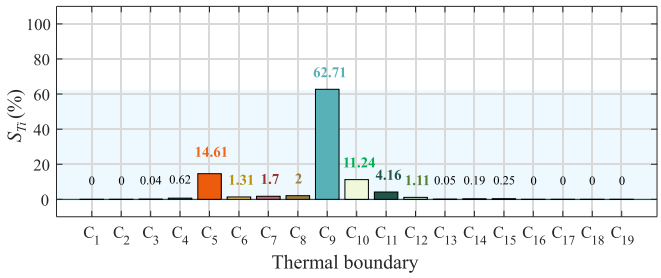

Fig. 15. Global sensitivity of uncertain thermal boundaries.

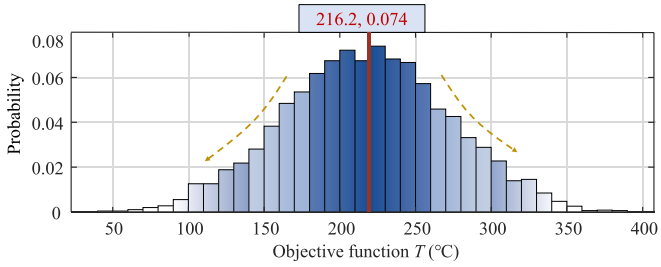

Fig. 16. Probability distribution of the second temperature objective function.

indices of these boundaries are 39.07 %, 9.08 %, 6.78 %, 17.77 %, 6.54 %, and 12.22 %, respectively. The close agreement between the first-order and global sensitivity indices confirms that boundaries C_3, C_5, C_7, C_9, C_{10}, and C_{15} exert the greatest influence on the output temperature.

The sensitivity analysis of the thermal boundaries for both temperature objective functions indicates that the uncertain boundaries C_3, C_5, C_7, C_9, C_{10}, and C_{15} encompass all high-sensitivity parameter types. Specifically, for the first temperature objective function, boundaries C_5, C_9, and C_{10} exhibit high sensitivity. For the second temperature objective function, boundaries C_3, C_5, C_7, C_9, C_{10}, and C_{15} are identified as highly sensitive parameters.

Boundaries C_3, C_5, C_7, and C_9 are directly exposed to high-temperature combustion gases, serving as the primary heat-receiving surfaces on the hot side of the rotor. These regions are subject to steep thermal gradients and intense convective heat transfer, which accounts for the significant influence of these sensitive boundaries on the temperature field distribution. In addition, boundaries C_{10} and C_{15} serve as relatively large cooling surfaces typically in contact with cool air. Their extensive surface areas and effective heat dissipation capacities play a crucial role in governing the overall thermal distribution.

5. High sensitivity thermal boundary prognostics of the assembled turbine rotor

In this section, the advanced WSO algorithm is first introduced. Next, an optimization objective function is defined based on experimental and simulation data. Finally, the WSO algorithm is used to inversely predict the high-sensitivity thermal boundaries of the T700 power turbine assembled rotor.

5.1. WSO algorithm

The WSO algorithm is a *meta*-heuristic algorithm inspired by the foraging behavior of great white sharks, particularly their exceptional auditory and olfactory sensing capabilities [44]. These biological behaviors are mathematically modeled to balance global exploration and local exploitation. By dynamically updating the positions of search agents relative to the best solutions currently found, WSO effectively avoids local minima and improves convergence toward the global optimum. The core principles of the algorithm are outlined as follows:

(1) When a white shark detects its prey through movement-induced fluctuations, it moves toward the prey in an undulating motion. This behavior can be described as follows:

$$v_{k+1}^{i} = \mu\left[v_k^i + p_1\left(w_{\text{gbest}k} - w_k^i\right) \times c_1 + p_2\left(w_{\text{best}}^{vi} - w_k^i\right) \times c_2\right] \tag{16}$$

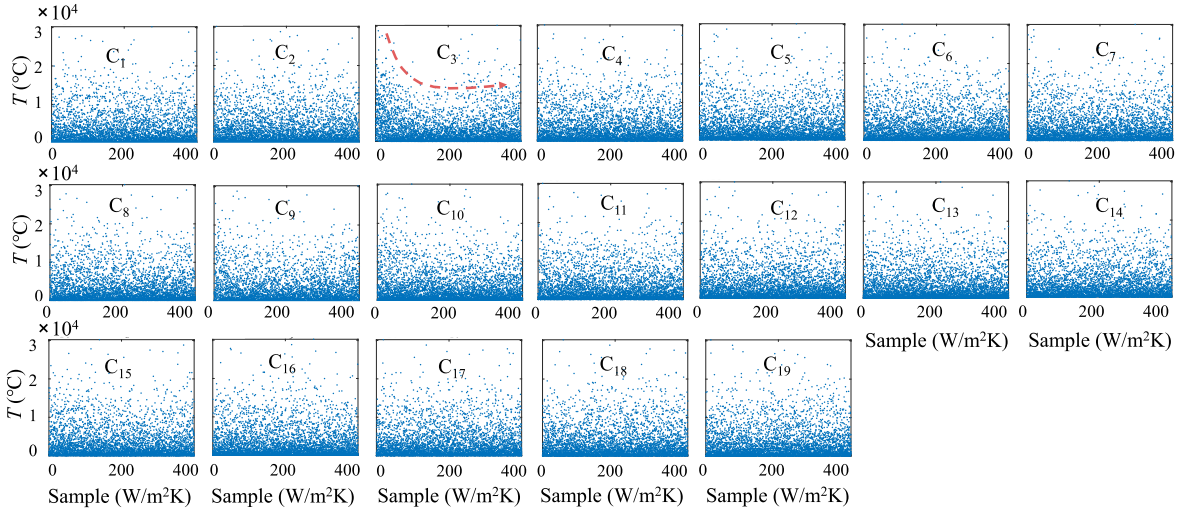

Fig. 17. Scatter plot of the second temperature objective function.

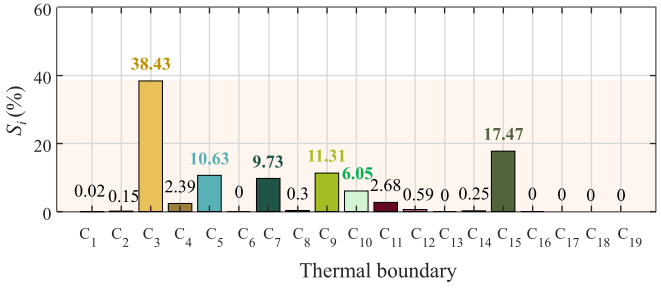

Fig. 18. First-order sensitivity of uncertain thermal boundaries.

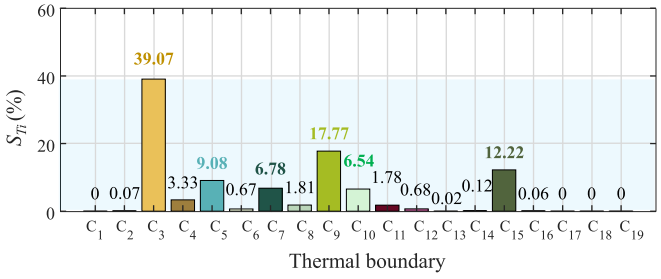

Fig. 19. Global sensitivity of uncertain thermal boundaries.

where i denotes the index of each white shark in a population of size. The new velocity vector of the i-th white shark at $(k+1)$-th step is denoted by v_{k+1}^i, while v_k^i, $w_{\text{gbest}k}$, and w_k^i represent its current velocity, the global best position, and current position at k-th step, respectively. The individual best position of the i-th white shark is denoted by w_{best}^{vi}. Random parameters c_1 and c_2 are drawn from the interval [0,1], while p_1 and p_2 control the influence of the global and individual best positions on the current position, respectively. μ is the contraction factor.

(2) Additionally, the white shark performs a random search for prey, described as follows:

$$w_{k+1}^i = \begin{cases} w_k^i \cdot \neg \oplus w_o + u \cdot a + l \cdot b, \text{ rand} < mv \\ w_k^i + \dfrac{v_k^i}{f}, \text{ rand} \geq mv \end{cases} \tag{17}$$

where w_{k+1}^i denotes the new position vector of the i-th white shark at $(k+1)$-th step, and $\neg$ is the negation operator. Variables l and u denote the lower and upper bounds of the search space, respectively. The one-dimensional binary vectors a and b are defined, and w_o is a logical vector. The parameter f represents the frequency of the white shark's movement, while rand denotes a random number uniformly distributed in [0,1]. The variable mv characterizes the sensory capabilities of the white shark, including its auditory and olfactory functions.

(3) Furthermore, white sharks move toward the individual closest to the best prey currently found, described as follows:

$$\acute{w}_{k+1}^i = w_{gbest_k} + r_1 D_w \text{sgn}(r_2 - 0.5), r_3 < s_s \tag{18}$$

where $\acute{w}_{k+1}^i$ is the updated position of the i-th white shark relative to the prey's position. Random variables r_1, r_2 and r_3 are uniformly distributed in [0,1]. D_w denotes the distance between the prey and white shark, and s_s represents the strength of the white shark's olfactory and visual senses when tracking nearby conspecifics close to the optimal prey.

To justify the adoption of the WSO, benchmark comparisons are performed against several widely used algorithms, including the sparrow search algorithm (SSA), particle swarm optimization (PSO), simulated annealing (SA), genetic algorithm (GA), whale optimization algorithm (WOA), improved grasshopper optimization algorithm (IGOA), artificial hummingbird algorithm (AHA), and artificial gorilla troops optimizer (GTO). These algorithms are evaluated for the task of estimating sensitive thermal boundary parameters in a complex assembled rotor structure. All comparisons are conducted under identical conditions, including the same objective function, optimization parameters, parameter bounds, and finite element model.

As shown in Fig. 20, the optimal objective values and computation times of different algorithms are assessed with a population size of 50 and a maximum of 40 iterations. The results indicate that, compared with the other algorithms, WSO exhibits strong overall performance in terms of both optimization accuracy and computational efficiency.

5.2. High sensitivity thermal boundary prognostics results

The optimization objective function for turbine rotor surface temperature, derived from both simulation and experimental data, is defined as follows:

$$f = min\left[10 \times \sum_{i=1}^{n} \left| T_{\text{sim}}(i) - T_{\text{exp}}(i) \right|\right] \tag{19}$$

where $T_{sim}(i)$ and $T_{exp}(i)$ denote the simulated and experimental tem-

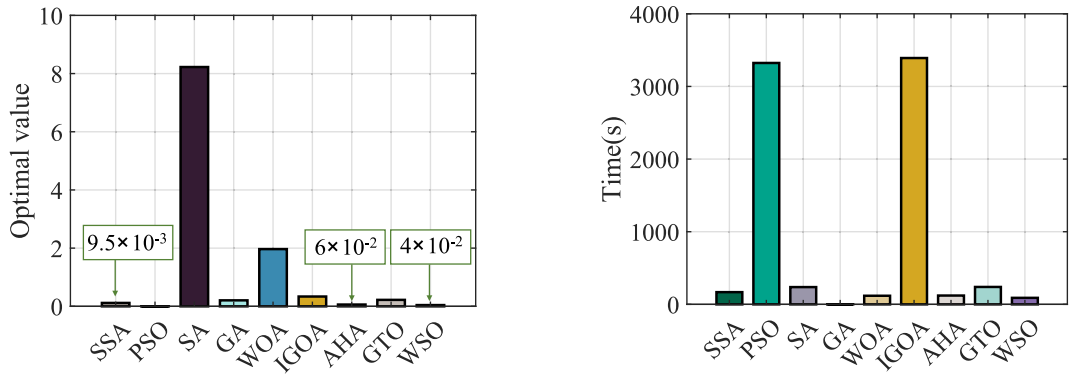

(a) Optimal objective function value (b) Time of calculation

Fig. 20. Evaluation of optimization algorithms.

peratures at the i th measurement point, respectively. As the optimization nears convergence, temperature differences may drop below 10^{-4}, causing the objective function values to become too small for effective convergence. To enhance numerical stability, a constant scaling factor of 10 is introduced into the objective function. Importantly, the scaling factor does not affect the location of the optimal solution but improves algorithmic stability. This practice is widely adopted in inverse optimization problems to ensure stable and accurate convergence.

Parameter optimization is conducted using three measurement points ($n = 3$), whose locations are shown in Fig. 21(a). These three points were selected for optimization because the actual turbine rotor structure is extremely compact, and the space available for installing temperature sensors is very limited. Generally, sensors are more easily installed near the turbine disk and drum, whereas placement near the shaft is more challenging. To evaluate the accuracy of the proposed sensitivity-driven thermal boundary prognostics method, the remaining six measurement points, shown in Fig. 21(b), are used to validate its applicability.

The WSO algorithm is employed to predict the high-sensitivity boundaries of the T700 power turbine assembled turbine rotor, using the optimized input parameters listed in Table 6. The range of 10–400 W/(m^2·K) is chosen based on physical constraints and empirical data, covering typical variations in convective heat transfer coefficients from standstill up to 12,000 rpm.

Fig. 22 shows the iterative results of the objective function obtained from four independent runs of the WSO algorithm under two cases. In both scenarios, the objective function exhibits a pronounced decrease as the number of iterations increases, eventually stabilizing at a constant value. This behavior indicates successful convergence of the algorithm. The consistent convergence behavior across multiple runs demonstrates the stability and repeatability of the WSO algorithm under these conditions. In addition, the proposed method involves three main computational steps: the temperature field simulation takes approximately 7.82 s per case, the global sensitivity analysis requires approximately 2.5 h, and the optimization process based on the WSO takes approximately 4300 s per case.

Table 6
Optimization parameters.

Parameter type	value
Population size	300
Maximum number of iterations	400
Number of high sensitivity parameters	6
Minimum thermal boundary parameter value (W/m^{2}K)	10
Maximum thermal boundary parameter value (W/m^{2}K)	400

Tables 7 and 8 show the predicted results of the six high-sensitivity parameters under Case 1 and Case 2, respectively. Notably, the thermal boundaries C_3, C_5, C_7, and C_{10} exhibit significant differences between the two operating conditions. These discrepancies arise from the notable variations in the heating structure between the two cases. As shown in Fig. 9, the difference in size of the cooling holes leads to distinct heat flow distributions and localized temperature gradients within the heating chamber, thereby altering local heat transfer efficiency. For instance, at C_7, which is located near the cooling holes, the heat transfer coefficient in Case 2 is significantly lower than in Case 1. This reduction is a result of enhanced airflow in the region, which rapidly removes heat and diminishes the local temperature gradient. In contrast, at locations less influenced by cooling (such as C_5), the heat transfer coefficient may increase slightly. Consequently, the observed variations in boundary condition parameters directly reflect the changes in the local thermal-fluid behavior induced by structural modifications.

The above predicted values are subsequently applied as boundary conditions in the temperature field model to obtain the temperature distribution of the assembled rotor. To validate the proposed method

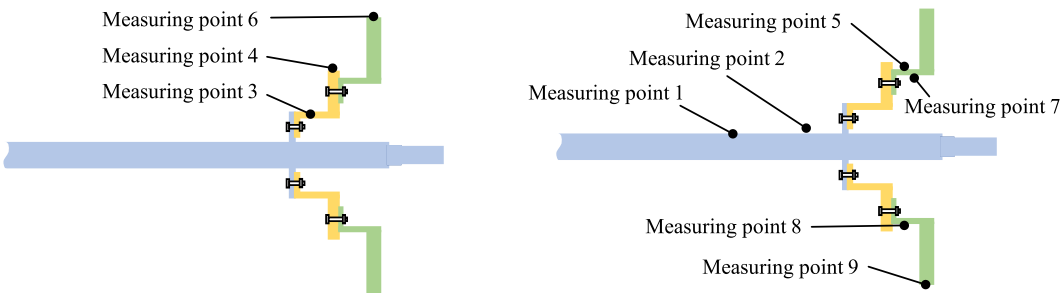

(a) For optimization (b) For verification

Fig. 21. Temperature measuring points.

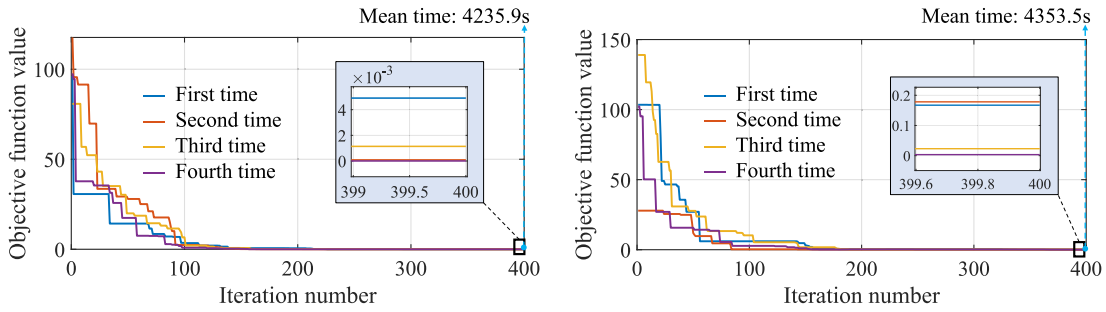

Fig. 22. Iteration results of objective function under two cases.

Table 7
Identification results under Case 1.

Parameter type	Value (W/m^{2}K)	Parameter type	Value (W/m^{2}K)
C_3	338.5	C_9	265.6
C_5	270.3	C_{10}	58.3
C_7	260.9	C_{15}	116.3

Table 8
Identification results under Case 2.

Parameter type	Value (W/m^{2}K)	Parameter type	Value (W/m^{2}K)
C_3	308.1	C_9	261.1
C_5	289.5	C_{10}	48.3
C_7	136.5	C_{15}	119.3

and evaluate its accuracy, the relative errors between the experimental and simulated temperatures at the measurement points shown in Fig. 21 (b) are calculated, as presented in Tables 9 and 10. In Case 1, the maximum and average relative errors among all measurement points are 2.5 % and 0.9 %, respectively. For Case 2, these values are 2.4 % and 1.5 %, respectively. Notably, the relative error is less than 3 % at all points for both cases, demonstrating high prediction accuracy.

To further demonstrate the advantages of the proposed method, predictions are performed for all uncertain boundaries. For a fair comparison, the same WSO optimization algorithm, identical optimization parameters (population size is 300 and maximum number of iterations is 400), and the experimental data from Case 1 are employed. Table 11 presents the experimental and simulated temperatures, together with their relative errors, when all thermal boundaries are predicted. It is evident that, under these consistent conditions, the prediction errors are significantly larger compared with those obtained when only high-sensitivity boundaries are predicted.

Table 9
Relative errors between experiment and simulation under Case 1.

Type	Experiment results (℃)	Simulation results (℃)	Relative errors (%)	Average relative error (%)
Measuring point 1	92.3	90.0	2.5 (maximum)	0.9
Measuring point 2	225.3	224.0	0.6	
Measuring point 5	251.0	252.9	0.8	
Measuring point 7	234.3	234.9	0.3	
Measuring point 8	250.7	252.9	0.9	
Measuring point 9	226.4	227.3	0.4	

Table 10
Relative errors between experiment and simulation under Case 2.

Type	Experiment results (℃)	Simulation results (℃)	Relative errors (%)	Average relative error (%)
Measuring point 1	77.1	78.4	1.7	1.5
Measuring point 2	216.1	218.3	1.0	
Measuring point 5	239.9	236.7	1.3	
Measuring point 7	227.9	222.5	2.4(maximum)	
Measuring point 8	242.2	236.7	2.3	
Measuring point 9	227.0	227.8	0.4	

Table 11
Relative errors between experiment and simulation under Case 1 (all uncertain boundaries are predicted).

Type	Experiment results (℃)	Simulation results (℃)	Relative error (%)
Measuring point 1	92.3	81.5	11.7
Measuring point 2	225.3	197.5	12.3
Measuring point 5	251.0	264.1	5.2
Measuring point 7	234.3	244.6	4.4
Measuring point 8	250.7	264.1	5.3
Measuring point 9	226.4	229.4	1.3

6. Conclusions and perspectives

In this work, a sensitivity-driven prognostic method for uncertain thermal boundaries in complex turbine rotor structures is proposed. The main conclusions are as follows:

(1) In modelling the turbine rotor temperature field, finite element models of the substructures are assembled using TCR at the bolted interfaces. A variance-based sensitivity analysis is conducted to evaluate both the first-order and global sensitivities of all uncertain boundaries, identifying C_3, C_5, C_7, C_9, C_{10}, and C_{15} as highly sensitive.

(2) An inverse prognostics approach integrating the WSO algorithm with sparse experimental data is proposed. Highly sensitivity boundary parameters are predicted under two cases. After the objective function's iterative curves converge, the predicted values are substituted into the temperature field model. The relative error between experimental and simulated results remains below 3 % in both cases, validating the

accuracy and effectiveness of the proposed method.

(3) This approach integrates the advantages of numerical modelling, statistical sensitivity analysis, and iterative optimization to achieve an efficient solution. A statistical sensitivity analysis identifies key parameters, enabling focused optimization while avoiding the computational burden of globally optimizing all uncertain boundaries. Crucially, the method requires only sparse experimental data, significantly reducing experimental costs and overcoming challenges associated with constrained testing conditions.

(4) A simplified assembled rotor is designed using dimensional analysis to provide preliminary validation of the proposed sensitivity-driven thermal boundary prognostics method. Although the design retains key geometric features and ensures that the dynamic response captures the fundamental characteristics of the actual rotor, details such as blades, blade roots, and seals are simplified in this structure. This simplification leads to some discrepancies compared with the real rotor. In the future, this method can be extended to a full-scale geometry to improve its engineering applicability.

(5) The proposed thermal boundary prognostics method is validated on a non-rotating turbine rotor structure. However, actual rotors operate under high-speed rotating conditions, where additional factors such as centrifugal effects and gyroscopic forces can influence heat transfer characteristics. Therefore, future work will include validation under realistic rotating conditions to comprehensively assess the method's applicability in practical engineering scenarios.

(6) The optimization objective function is based on the mean squared error of temperature. Future work aims to incorporate local temperatures at critical regions, such as bolt joints, blade roots, and couplings, to enable multi-objective optimization and better meet broader engineering requirements. Additionally, to improve the accuracy and robustness of boundary prediction, the number of temperature measurement points will be increased, and weighting factors will be introduced into the objective function.

(7) Considering the spatial limitations of the actual rotor structure, three temperature measurement points distributed on the rotor disk and drum are used for optimization calculations. Although the final prediction results in this work demonstrate high accuracy, a thorough quantitative analysis of how the number and placement of temperature measurement points used for optimization affect prediction accuracy and computational speed was not conducted. Quantitative analysis of these factors require further improvement in future work.

CRediT authorship contribution statement

Yazheng Zhao: Writing – original draft, Funding acquisition, Data curation, Conceptualization. **Yang Zhou:** Data curation. **Yulin Jiang:** Validation. **Jin Zhou:** Writing – review & editing, Supervision, Funding acquisition. **Yuanping Xu:** Writing – review & editing, Supervision. **Chaofeng Li:** Writing – review & editing, Supervision.

Declaration of competing interest

The authors declare that they have no known competing financial interests or personal relationships that could have appeared to influence the work reported in this paper.

Acknowledgement

This work was supported by the National Natural Science Foundation of China (Grant No. 52475060), the Nanjing University of Aeronautics and Astronautics State Key Laboratory of Mechanics and Control for Aerospace Structures (Grant No. MCAS-S-0425G02), and the Outstanding Doctoral Dissertation Funding of NUAA (Grant No. BCXJ25-13). We sincerely appreciate the valuable support provided by the editor and reviewers.

Appendix A

The thermal conductivity matrix, heat capacity matrix, and temperature load vector are as follows:

$$\boldsymbol{K}(h)^E = \begin{bmatrix} \phi^{'}\left(b_j^2 + c_j^2\right) & \phi^{'}\left(b_i b_j + c_i c_j\right) & \phi^{'}\left(b_i b_m + c_i c_m\right) \\ \phi^{'}\left(b_i b_j + c_i c_j\right) & \phi^{'}\left(b_j^2 + c_j^2\right) + \dfrac{hs_i}{4}\left(r_j + \dfrac{r_m}{3}\right) & \phi^{'}\left(b_j b_m + c_j c_m\right) + \dfrac{hs_i}{12}\left(r_j + r_m\right) \\ \phi^{'}\left(b_i b_m + c_i c_m\right) & \phi^{'}\left(b_j b_m + c_j c_m\right) + \dfrac{hs_i}{12}\left(r_j + r_m\right) & \phi^{'}\left(b_m^2 + c_m^2\right) + \dfrac{hs_i}{4}\left(r_m + \dfrac{r_j}{3}\right) \end{bmatrix} \tag{A1}$$

$$\boldsymbol{N}^E = \begin{bmatrix} \dfrac{\Delta}{30}\rho c_p\left(3r_i + r_j + r_m\right) & \dfrac{\Delta}{60}\rho c_p\left(2r_i + 2r_j + r_m\right) & \dfrac{\Delta}{60}\rho c_p\left(2r_i + r_j + 2r_m\right) \\ \dfrac{\Delta}{60}\rho c_p\left(2r_i + 2r_j + r_m\right) & \dfrac{\Delta}{30}\rho c_p\left(r_i + 3r_j + r_m\right) & \dfrac{\Delta}{60}\rho c_p\left(r_i + 2r_\gamma + 2r_m\right) \\ \dfrac{\Delta}{60}\rho c_p\left(2r_i + r_j + 2r_m\right) & \dfrac{\Delta}{60}\rho c_p\left(r_i + 2r_\gamma + 2r_m\right) & \dfrac{\Delta}{30}\rho c_p\left(r_i + r_j + 3r_m\right) \end{bmatrix} \tag{A2}$$

$$\boldsymbol{P}(h)^E = \begin{bmatrix} \dfrac{\Delta}{12}q_v\left(2r_i + r_j + r_m\right) \\ \dfrac{\Delta}{12}q_v\left(r_i + 2r_j + r_m\right) + \dfrac{hs_i T_f}{3}\left(r_j + \dfrac{r_m}{3}\right) \\ \dfrac{\Delta}{12}q_v\left(r_i + r_j + 2r_m\right) + \dfrac{hs_i T_f}{3}\left(r_j + \dfrac{r_m}{3}\right) \end{bmatrix} \tag{A3}$$

where the unknown parameter where the coefficient $\phi^{'}$ is expressed as $\phi^{'} = k(r_i + r_j + r_m)/(12\Delta)$, Δ is equal to $b_i c_j + b_j c_i$. The coefficients $a_i, b_i, c_i, a_j, b_j, c_j, a_m, b_m, c_m$ are undetermined, they are obtained based on the node coordinates:

$$\begin{array}{lll} a_i = r_j z_m - r_m z_j & b_i = z_j - z_m & c_i = r_m - r_j \\ a_j = r_m z_i - r_i z_m & b_j = z_m - z_i & c_j = r_i - r_m \\ a_m = r_i z_j - r_j z_i & b_m = z_i - z_j & c_m = r_j - r_i \end{array} \tag{A4}$$

where the position coordinates of the three nodes i, j and m of an element are defined as (r_i, z_i), (r_j, z_j), (r_m, z_m) respectively.

Appendix B

The truncated area, maximum truncated area, critical truncated area, and minimum truncated area of the asperity are expressed as:

$$\begin{cases} a_{tmax} = A_t {D_f}^{-1} \left(2 - D_f\right) \varphi^{\frac{D_f - 2}{2}} \\ a_{tc} = 2 {G_f}^2 \left(\dfrac{\widetilde{H}}{2\widetilde{E}}\right)^{\frac{2}{1 - D_f}} \\ a_s = 10^{-18} \end{cases} \tag{B1}$$

where D_f and G_f denote the fractal dimension and fractal roughness, respectively. $\widetilde{H}$ and $\widetilde{E}$ represent the equivalent hardness and elastic modulus of the contact surface. φ is the domain expansion factor, satisfying the equation $\varphi^{(2-D_f)/2} - \left(1 + \varphi^{-1/2D_f}\right)^{1-2/D_f} - 2/D_f + 1 = 0, D_f \in (1, 2)$.

$$n(a_t) = \frac{1}{2} D_f \varphi^{\frac{2 - D_f}{2}} a_{tmax}^{\frac{D_f}{2}} a_t^{-\frac{D_f + 2}{2}}, a_t \in [0, a_{tmax}] \tag{B2}$$

$$\begin{cases} A_a = \pi r_m^2 - \pi \left(\dfrac{\alpha d}{2}\right)^2 \\ A_r = \dfrac{1}{2} \displaystyle\int_0^{a_{tmax}} a_t n(a_t) da_t \\ A_t = \displaystyle\int_0^{a_{tmax}} a_t n(a_t) da_t \end{cases} \tag{B3}$$

where α denotes the diameter coefficient of the bolt hole, d represents the nominal diameter of the bolt, and r_m is the distance from the center of the bolt hole to the stress field boundary.

Appendix C

The independent sampling matrices $\boldsymbol{A}$ and $\boldsymbol{B}$ are denoted as follows:

$$A = \begin{bmatrix} a_{1,1} & \cdots & a_{1,k} \\ \vdots & \ddots & \vdots \\ a_{N,k} & \cdots & a_{N,k} \end{bmatrix}, B = \begin{bmatrix} b_{1,1} & \cdots & b_{1,k} \\ \vdots & \ddots & \vdots \\ b_{N,k} & \cdots & b_{N,k} \end{bmatrix} \tag{C1}$$

where a_{ji} and b_{ji} are general elements of the respective matrices.

The matrix ${\boldsymbol{A}_{\boldsymbol{B}}}^{(i)}$ associated with the i th factor C_i obtained by radial resampling method is as follows:

$${\boldsymbol{A}_{\boldsymbol{B}}}^{(i)} = \begin{bmatrix} a_{1,1} & \cdots & a_{1,i-1} & b_{1,i} & a_{1,i+1} & \cdots & a_{1,k} \\ \vdots & & & \ddots & & & \vdots \\ a_{N,k} & \cdots & a_{N,i-1} & b_{N,i} & a_{N,i+1} & \cdots & a_{N,k} \end{bmatrix} \tag{C2}$$

Data availability

The original simulation data and experimental measurement data supporting the findings of this study will be made available on request.

References

[1] Lin AQ, Liu GW, Yu XX, et al. Comprehensive investigations on fluid flow and heat transfer characteristics of a high-speed rotating turbine disk cavity system of aero-engine. Int Commun Heat Mass Transfer 2022;136:106170.

[2] Zhao YZ, Zhou J, Guo MJ, et al. Environmental-structural-structural heat transfer characteristics analysis of an assembled power turbine rotor system. Int J Heat Mass Transf 2025;240:126639.

[3] Rusin A, Nowak G, Łukowicz H, et al. Selecting optimal conditions for the turbine warm and hot start-up. Energy 2020;214:118836.

[4] Owen JM, Long CA. Review of Buoyancy-Induced Flow in Rotating Cavities. J Turbomach 2015;137(11):111001.

[5] Farahani SD, Mahdi SK. Experimental estimation of temperature-dependent thermal conductivity coefficient by using inverse method and remote boundary condition. Int Commun Heat Mass Transfer 2020;117:104736.

[6] Casto A, Vittucci M, Vialla F, et al. Experimental optical retrieval of the thermal Boundary Resistance of carbon nanotubes in water. Carbon 2024;229:119445.

[7] Zhu FD, Chen JC, Han YG, et al. A deep learning method for estimating thermal boundary condition parameters in transient inverse heat transfer problem. Int J Heat Mass Transf 2022;194:123089.

[8] Adnan KZ, Neupane MR, Feng T. Thermal boundary conductance of metal–diamond interfaces predicted by machine learning interatomic potentials. Int J Heat Mass Transf 2024;235:126227.

[9] Zhan TZ, Fang L, Xu YB. Prediction of thermal boundary resistance by the machine learning method. Sci Rep 2017;7(1):7109.

[10] Li XQ, Song LK, Bai GC. Deep learning regression-based stratified probabilistic combined cycle fatigue damage evaluation for turbine bladed disk. Int J Fatigue 2022;159:106812.
[11] Song LK, Bai GC, Li XQ. A novel metamodeling approach for probabilistic LCF estimation of turbine disk. Eng Fail Anal 2021;120:105074.
[12] Liao GL, Liu LJ, Zhang F, et al. A comparison of numerical investigations on the flow and heat transfer characteristics in the rotor-stator cavity. Appl Therm Eng 2019;162:114231.
[13] Hölz P, Böhlke T, Krämer T. Fast algorithms for generating thermal boundary conditions in combustion chambers. Appl Therm Eng 2018;141:101–13.
[14] Martins IT, Matsuda VA, Cabezas-Gómez L. A new Neumann boundary condition scheme for the thermal lattice Boltzmann method. Int Commun Heat Mass Transfer 2024;156:107653.
[15] Heinze T. Constraining the heat transfer coefficient of rock fractures. Renew Energy 2021;177:433–47.
[16] Battaglia JL. Linear and non-linear thermal system identification based on the integral of non-integer order—Application to solve inverse heat conduction linear and non-linear problems. Int J Therm Sci 2024;197:108840.
[17] Li BY, Zhang JX, Cheng JP, et al. An analytical solution to periodical heat transfer problems of multilayer rocks for thermal energy storage in underground mines. J Storage Mater 2022;50:104320.
[18] Liu Y, Mitsutake YC, Masanori M. Analytical solution to the two-dimensional inverse heat conduction problem in an axisymmetric cylindrical coordinate system. Int J Therm Sci 2024;206:109335.
[19] Yang ZQ, Cui JZ, Sun Y. Transient heat conduction problem with radiation boundary condition of statistically inhomogeneous materials by second-order two-scale method. Int J Heat Mass Transf 2016;100:362–77.
[20] Gaaloul N, Daouas N. An extended approach of a Kalman smoothing technique applied to a transient nonlinear two-dimensional inverse heat conduction problem. Int J Therm Sci 2018;134:224–41.
[21] Da Silva WB, Dutra JCS, Kopperschimidt CEP, et al. Sequential particle filter estimation of a time-dependent heat transfer coefficient in a multidimensional nonlinear inverse heat conduction problem. App Math Model 2021;89:654–68.
[22] Wang XW, Li HP, He LF, et al. Evaluation of multi-objective inverse heat conduction problem based on particle swarm optimization algorithm, normal distribution and finite element method. Int J Heat Mass Transf 2018;127:1114–27.
[23] Song LK, Tao F, Li XQ, Yang LC, Wei YP, Beer M. Physics-embedding multi-response regressor for time-variant system reliability assessment. Reliab Eng Syst Saf 2025;263:111262.
[24] Ren T, Mu HP, Liu S, et al. Prediction of gas-liquid two-phase heat transfer coefficient. Appl Therm Eng 2017;116:217–32.
[25] Chen HL, Yu B, Zhou HL, et al. Identification of transient boundary conditions with improved cuckoo search algorithm and polynomial approximation. Eng Anal Bound Elem 2018;95:124–41.
[26] Tourn BA, Hostos JCÁ, Fachinotti VD. A modified sequential gradient-based method for the inverse estimation of transient heat transfer coefficients in non-linear one-dimensional heat conduction problems. Int Commun Heat Mass Transfer 2021;127:105488.
[27] Chen SY, Li YZ, Fu JW, et al. Reconstruction of transient convective heat transfer coefficients in heat transfer of gun barrels with variable coefficients. Case Stud Therm Eng 2023;50:103467.
[28] Cui M, Mei J, Zhang BW, et al. Inverse identification of boundary conditions in a scramjet combustor with a regenerative cooling system. Appl Therm Eng 2018;134:555–63.
[29] Duda P. A general method for solving transient multidimensional inverse heat transfer problems. Int J Heat Mass Transf 2016;93:665–73.
[30] Han WW, Chen HB, Lu T. Estimation of the time-dependent convective boundary condition in a horizontal pipe with thermal stratification based on inverse heat conduction problem. Int J Heat Mass Transf 2019;132:723–30.
[31] Chakraborty S, Ganguly S, Chacko EZ, et al. Estimation of surface heat flux in continuous casting mould with limited measurement of temperature. Int J Therm Sci 2017;118:435–47.
[32] Frąckowiak A, Wróblewska A, Ciałkowski M. Trefftz numerical functions for solving inverse heat conduction problems. Int J Therm Sci 2022;177:107566.
[33] Mierzwiczak M, Kołodziej JA. Application of the method of fundamental solutions and radial basis functions for inverse transient heat source problem. Comput Phys Commun 2010;181(12):2035–43.
[34] Wang Y, Qian Z. A quasi-reversibility method for solving a two-dimensional time-fractional inverse heat conduction problem. Math Comput Simul 2023;212:423–40.
[35] Bauzin JG, Cherikh MB, Laraqi N. Identification of thermal boundary conditions and the thermal expansion coefficient of a solid from deformation measurements. Int J Therm Sci 2021;164:106868.
[36] Adams C, Bös J, Slomski EM, et al. Scaling laws obtained from a sensitivity analysis and applied to thin vibrating structures. Mech Syst Sig Process 2018;110:590–610.
[37] Luo Z, Zhu Y, Zhao X, et al. Determining dynamic scaling laws of geometrically distorted scaled models of a cantilever plate. J Eng Mech 2016;142(4):04015108.
[38] Greś S, Döhler M, Mevel L. Uncertainty quantification of the modal assurance criterion in operational modal analysis. Mech Syst Sig Process 2021;152:107457.
[39] Zhao YZ, Zhou J, Guo MJ, et al. Equivalent thin-layer temperature field model (ETTM) for bolted rotors to describe interface temperature jump. Int J Heat Mass Transf 2024;222:125086.
[40] Zhou Y, Xu Y, Zhou J, et al. Numerical and experimental investigations on the dynamic behavior of a rotor-AMBs system considering shrink-fit assembly. Mech Syst Sig Process 2025;224:111980.
[41] Li D, Botto D, Li R, et al. Experimental and theoretical studies on friction contact of bolted joint interfaces. Int J Mech Sci 2022;236:107817.
[42] Pan W, Li X, Wang L, et al. A normal contact stiffness fractal prediction model of dry-friction rough surface and experimental verification. Eur J Mech A Solids 2017;66:94–102.
[43] Saltelli A, Annoni P, Azzini I, et al. Variance based sensitivity analysis of model output. Comput Phys Commun 2010;181:259–70.
[44] Braik M, Hammouri A, Atwan J, et al. White shark optimizer: a novel bio-inspired meta-heuristic algorithm for global optimization problems. Knowl-Based Syst 2022;243:108457.